Imaging the Kanto Basin bedrock with noise and earthquake autocorrelations

Loïc Viens[1], Chengxin Jiang[2], and Marine Denolle[3]

[1]Disaster Prevention Research Institute, Kyoto University
[2]Australian National University
[3]Harvard University

November 21, 2022

Abstract

Sedimentary basins can strongly amplify seismic waves from earthquakes. To better predict strong ground motions, thorough knowledge of sediment thickness and internal basin structure is required. This study maps the deep and complex bedrock shape of the Kanto Basin, Japan, using ambient seismic noise and earthquake autocorrelation functions (ACFs). Noise ACFs are computed using one month of continuous data recorded by the vertical component of 287 MeSO-net stations located in the greater Tokyo area. Earthquake ACFs are obtained from the P-wave records at the MeSO-net stations of 50 Mw 6+ teleseismic earthquakes. Both noise and earthquake ACFs exhibit great similarity in P-wave reflections, confirming that the same wavefield is extracted with both methods. We finally map the basin bedrock geometry and find that it is comparable with that from an existing 3-D velocity model.

Posted on 21 Nov 2022 — The copyright holder is the author/funder. All rights reserved. No reuse without permission. — https://doi.org/10.1002/essoar.10504543.1 — This a preprint and has not been peer reviewed. Data may be preliminary.

Imaging the Kanto Basin bedrock with noise and earthquake autocorrelations

Loïc Viens[1], Chengxin Jiang[2], and Marine A. Denolle[3]

[1]Disaster Prevention Research Institute, Kyoto University, Uji, Japan
[2]Research School of Earth Sciences, The Australian National University, Canberra, ACT, Australia
[3]Department of Earth and Planetary Sciences, Harvard University, Cambridge, MA, USA

Key Points:

- Noise and earthquake autocorrelation functions from a dense seismic network are used to map the bedrock depth of the Kanto Basin, Japan
- Both methods recover similar P-wave reflections from the basin bedrock
- Our study is the first urban-basin-scale mapping of a complex seismic basement using passive data from a dense seismic network

Corresponding author: Loïc Viens, `viens.loic.58r@st.kyoto-u.ac.jp`

Abstract

Sedimentary basins can strongly amplify seismic waves from earthquakes. To better predict strong ground motions, thorough knowledge of sediment thickness and internal basin structure is required. This study maps the deep and complex bedrock shape of the Kanto Basin, Japan, using ambient seismic noise and earthquake autocorrelation functions (ACFs). Noise ACFs are computed using one month of continuous data recorded by the vertical component of 287 MeSO-net stations located in the greater Tokyo area. Earthquake ACFs are obtained from the P-wave records at the MeSO-net stations of 50 $\mathrm{M_w}$ 6+ teleseismic earthquakes. Both noise and earthquake ACFs exhibit great similarity in P-wave reflections, confirming that the same wavefield is extracted with both methods. We finally map the basin bedrock geometry and find that it is comparable with that from an existing 3-D velocity model.

Plain Language Summary

Sedimentary basins, which lie beneath numerous urban areas, can significantly increase seismic hazard by amplifying incoming seismic waves from earthquakes. This study focuses on the deep and complex Kanto Basin, Japan, which is well known to amplify long-period ground motions that are a potential threat to the numerous urban infrastructures of the greater Tokyo area. We combine measurements from ambient seismic noise and earthquake records at seismic stations of a dense network to derive a map of the sedimentary basin bedrock. We find that both methods yield similar results, which had not been reported before, and that they can be used to infer the geometry of the complex Kanto Basin.

1 Introduction

Sedimentary basins have the potential to strongly amplify and extend the duration of seismic waves from earthquakes, which can pose a threat to urban infrastructures (Anderson et al., 1986; Koketsu & Kikuchi, 2000; Koketsu et al., 2005). The Kanto Basin, Japan, is a large-scale sedimentary structure that underlies the highly populated greater Tokyo area. The basin has a sediment-to-bedrock interface that is locally deeper than 4 km (Figure 1a) and is well known to amplify long-period seismic waves (e.g., Denolle et al., 2014; Furumura & Hayakawa, 2007; Kudo, 1978, 1980; Mamula et al., 1984; Viens et al., 2016). During the last decade, several velocity models have been constructed from various geological and geophysical datasets and have revealed the complex bedrock shape and the internal structure of the basin (Fujiwara et al., 2012; Koketsu et al., 2012; Yamada & Yamanaka, 2012). Among these models, the Japan Integrated Velocity Structure Model (JIVSM, Koketsu et al., 2008, 2012) divides the basin into three layers with P- and S-wave velocities increasing with depth. While the JIVSM is a recent and well used velocity model, seismic wave simulations showed that the model cannot fully explain the long-period ground motions from earthquakes (Takemura et al., 2015; Yoshimoto & Takemura, 2014).

Active seismic surveys are generally used to obtain high-resolution images of the Earth's shallow subsurface, but are expensive and rather impractical in urban areas (Morrice et al., 2001). During the past two decades, passive seismic methods have become very popular to map shallow structures using dense seismic networks. For example, the receiver function (Langston, 1979; Leahy et al., 2012; Liu et al., 2018) and horizontal-to-vertical (H/V) spectral ratio (Guéguen et al., 2007; Nakamura, 1989) methods have been used to obtain detailed images of sedimentary basins. However, both techniques require 3-component seismometers, which are not yet fully standard for temporary station deployments.

Autocorrelation functions (ACFs) of vertical seismic noise records can be used to retrieve the P-wave reflectivity response of the underlying medium, from which the geometry of the structure can then be inferred. The theoretical framework of the method was first introduced by Claerbout (1968) for acoustic waves in 1-D media and later extended to 3-D media (Wapenaar, 2003). Noise ACFs are particularly powerful to image interfaces with strong seismic impedance contrasts, such as sedimentary basin bedrocks (Clayton, 2020; Romero & Schimmel, 2018; Saygin et al., 2017), the Mohorovičić (Moho) discontinuity (Clayton, 2020; Gorbatov et al., 2013; Oren & Nowack, 2016; Tibuleac & von Seggern, 2012), and subducting slabs (Ito et al., 2012).

ACFs can also be computed using P-waves (and their coda) from teleseismic events (e.g., Pham & Tkalčić, 2017). This method takes advantage of the near vertical incidence of teleseismic P-waves beneath seismometers to retrieve the P-wave reflectivity response of the underlying medium. Earthquake ACFs have been used to image shallow structures such as ice sheets (Pham & Tkalčić, 2017; Phạm & Tkalčić, 2018), the crust structure (Delph et al., 2019; Tork Qashqai et al., 2019), and the Moho discontinuity (Delph et al., 2019; Pham & Tkalčić, 2017; Tork Qashqai et al., 2019), as well as deep structures such as the Earth's inner core (Huang et al., 2015; Wang et al., 2015).

One major difference between the noise and earthquake ACF methods resides in the nature of the wavefield that is correlated (Tkalčić et al., 2020). While P-waves and their coda from teleseismic earthquakes arrive with an almost vertical incidence angle beneath seismic stations, the seismic noise is mainly generated at the Earth's surface by the coupling of oceans with the solid Earth at long periods (> 1 s) and human activities at short periods (< 1 s). This results in a noise wavefield that is generally dominated by surface waves and that only contains weak body wave energy (Bonnefoy-Claudet et al., 2006; Clayton, 2020). Practically, the different nature of the wavefield affects the convergence of the ACFs. Days-to-weeks of continuous records can be necessary to retrieve a clear P-wave reflectivity response using noise ACFs, whereas the P-wave ACFs from only a few teleseismic events can yield an accurate response of the medium (e.g., Lin & Tsai, 2013, for a station-to-station correlation setting). Physically, the different nature of the signals that are autocorrelated challenges the interpretation of the extracted seismic wavefield.

To our best knowledge, the literature currently lacks a comparison of the P-wave reflectivity response obtained by both ambient noise and earthquake P-wave coda ACFs. This study fills this gap by taking advantage of a dense seismic network to map the complex Kanto Basin bedrock with both methods. We show that despite having different waveform shapes, both noise and earthquake ACFs can be used to image the bedrock depth. We finally compare our results with the JIVSM and discuss the different features obtained with both the noise and earthquake ACFs.

2 Data and Methods

2.1 Noise ACFs

We use 30 days of data recorded by 287 accelerometers of the Metropolitan Seismic Observation network (MeSO-net, Kasahara et al., 2009; Sakai & Hirata, 2009) from January 1 to 15 and July 1 to 15, 2019. The sensors are buried in 20-m deep boreholes and shown in Figure 1a. The data are first band-pass filtered between 0.05 and 5 Hz (4-pole 2-pass Butterworth bandpass filters are used for all filtering operations), corrected for their instrument response, down-sampled from 200 Hz to 20 Hz, and split into 20-min time series. Each 20-min acceleration waveform is then zero-padded to four times its original length and noise ACFs are calculated in the frequency domain (ω) as

$$\mathrm{ACF}_{Z,Z}(t) = F^{-1}(\hat{a}_Z(\omega)\hat{a}^*_Z(\omega)), \tag{1}$$

where $\hat{a}$ is the Fourier transform of a vertical (Z) zero-padded 20-min acceleration record. The $*$ symbol is the complex conjugate and F^{-1} is the inverse Fourier transform applied to retrieve ACFs in the time domain (represented by t). For each station, the stacking of noise ACFs is performed after rejecting 20-min ACFs with potentially overwhelming amplitudes that would dominate the stack. To do so, we compute a metric as the sum of the mean and the standard deviation of all the 20-min ACF absolute peak amplitudes. Then, we only stack the 20-min ACFs with absolute peak amplitudes smaller than the metric using the phase-weighted stack (PWS, Schimmel & Paulssen, 1997) method (power: 2 and smoothing: 0.1 s). Finally, we band-pass filter the stacked ACFs between 1 and 10 s and only consider the causal part of the ACFs given their strict symmetry. To demonstrate that seasonality has little influence on the noise ACF stability, we show a comparison of the noise ACFs computed either from the data recorded in January or from July in Supplementary Material Figure S1.

To remove the effect of the source function (e.g., zero-time lag spike) and enhance the contribution of the reflectivity response of the medium, we follow the procedure introduced by Clayton (2020). For each station, we subtract the noise ACF with a linear average of all ACFs within a 25-km radius of the site. The 25-km radius is chosen empirically as a trade off between spatial resolution and number of ACFs to average (i.e., number of surrounding stations). We exclude stations/sites with fewer than 10 ACFs to average within that radius to ensure the stability of the average trace. An example of the average trace removal process is shown in Supplementary Material Figure S2. Finally, the noise ACFs are normalized by their absolute peak amplitude.

2.2 Earthquake ACFs

To compute earthquake ACFs, we select 244 $\mathrm{M_w}$ 6+ earthquakes which occurred between May 2017 and April 2020 within 30 and 95 degrees of angular distance from the Kanto Basin using the USGS (National Earthquake Information Center, NEIC) catalog (Figure 1b). For each earthquake, we download 120 s-long vertical waveforms at the MeSO-net stations with a 20 Hz sampling rate, starting 20 s before the predicted direct P-wave arrival calculated using the AK135 model (Kennett et al., 1995). We then select earthquakes with signal-to-noise ratio (SNR) values averaged over the 287 MeSO-net stations larger than 2.5. The SNR is defined as the ratio of the peak absolute amplitude within a 6 s window after the direct P-wave divided by the root-mean-square of a 15 s noise window starting 20 s before the direct P-wave. Finally, we remove a few of the selected events with no clear P-wave onsets after visual inspection. The final selection contains the 50 events shown in Figure 1b.

To compute ACFs from P-waves and their coda, we follow the procedure described in Pham and Tkalčić (2017). For each earthquake, we correct the data for their instrument response, select a 45 s-long window starting 15 s before the P-wave arrival, and remove both the mean and trend of the data. Similarly to noise ACFs, earthquake ACFs are computed in the frequency domain after zero-padding the data to four times their initial duration. The only difference is that the earthquake spectra are pre-whitened after being Fourier transformed to mitigate biases towards low frequencies that dominate the earthquake spectra (Pham & Tkalčić, 2017). Data pre-whitening is performed using the running-mean average algorithm of Bensen et al. (2007) with a sliding-spectral window of 30 samples (i.e., 0.67 Hz). The length of the sliding-spectral window does not considerably impact the time-domain ACFs (Supplementary Material Figure S3). After applying the inverse Fourier transform, the time-domain ACFs are tapered with a 10-sample (i.e., 0.5 s) Tukey window to suppress the zero-time-lag spikes and are band-pass filtered between 1 and 10 s. Finally, the PWS algorithm (power: 2 and smoothing: 0.1 s) is applied to stack the ACFs from the 50 earthquakes. Similarly to noise ACFs, only the causal part is analyzed and the waveforms are normalized by their absolute peak amplitudes. Note that the average trace removal step is not performed for the earthquake ACFs.

3 Results and discussion

We show the noise and earthquake ACFs along Lines 1 to 4 (locations in Figure 1a) together with the corresponding JIVSM velocity profiles in Figures 2 and 3. For each station, we first use the JIVSM to compute three theoretical arrival times of P-waves traveling between the surface and the bedrock interface (Figure 2b). The 2p arrival time corresponds to a P-wave traveling from the station down to the bedrock interface and back up to the station. The $2p^2$ and $2p^3$ arrival times are twice and three times the down-then-up path and therefore have their arrival times being twice and three times that of 2p, respectively.

Along the four lines, noise ACFs show clear negative phases near the theoretical 2p and $2p^3$ arrival times and positive phases near the $2p^2$ arrivals (e.g., Figures 2b, 2f, 3b, and 3f). The polarity changes for the $2p^2$ and $2p^3$ phases are caused by free-surface reflections. Earthquake ACFs primarily exhibit consistent negative phases near the theoretical 2p arrival time (Figures 2c, 2g, 3c, and 3g). Moreover, clear positive phases near the theoretical $2p^2$ arrival time can also be observed at some stations along Lines 1–3 (Figures 2c, 2g, and 3c). The stations that exhibit strong multiples for both noise and earthquake ACFs are generally located in the area where the four lines intersect.

In the following, we focus on the negative phases near the theoretical $2p^3$ and 2p arrival times for the noise and earthquake ACFs, respectively. For the noise ACFs, the phases near the theoretical $2p^3$ arrival time are more stable than that near the 2p and $2p^2$ arrival times. This can be explained by the fact that the 2p and $2p^2$ arrival times are closer to the zero time lag and therefore more likely to be affected by the average trace removal process and/or by potential weak reflections from the three internal layers of the basin. To measure the travel time of the $2p^3$ phase from noise ACFs, we simply select the negative peak values between the theoretical $2p^3$ arrival time ± 2.5 s. If several negative peaks are found within the empirically chosen 5-s window, we select the negative peak that is the closest to the theoretical $2p^3$ arrival time. Note that we also visually inspect the waveforms to manually adjust a few values (list of manually adjusted stations in Supplementary Material Table S1).

The selected travel times are finally divided by three to retrieve the P-wave two-way travel times shown in Figures 2d, 2h, 3d, and 3h. For the earthquake ACFs, we select the negative peaks within the theoretical 2p phase $\pm$ 0.65 s. For both methods, no value is assigned if there is no negative peak within the considered time windows (e.g., Figure 3b at 58 km).

Along Lines 1 and 2, the bedrock depth varies relatively smoothly along the lines and we obtain P-wave two-way travel time values from both the noise and earthquake ACFs that are consistent with the theoretical 2p arrival times (Figures 2d and 2h). Along Line 3, which crosses the western basin edge, the bedrock depth changes more rapidly (Figure 3a). This leads to slightly more complex noise and earthquake ACFs, especially near the deepest part of the basin along the line. Nevertheless, the measured P-wave two-way travel time values from both methods agree well with that predicted from the JIVSM. Along Line 4, which has its southern end close to the Sagami Trough, noise and earthquake ACFs are also relatively complex (Figures 3f and 3g). For the first 20 km along Line 4, the bedrock depth from the JIVSM rapidly increases from 1.5 km to 3 km (Figure 3e). While the measured P-wave two-way travel times from the noise and earthquake ACFs seem to agree with that from the JIVSM, the autocorrelograms in Figures 3f and 3g do not exhibit clear phases of such depth variations. Between 20 and 50 km from the south-western end of Line 4, there is a rather large discrepancy between the two types of ACFs, with clear negative phases near the theoretical 2p arrival time for the earthquake ACFs compared to the weak amplitude of the noise ACFs near the theoretical $2p^3$ arrival time. Moreover, the measured P-wave two-way travel times computed from earthquake ACFs are shorter than that from the noise ACFs and the JIVSM for this part of Line 4 (Figure 3h). We show in Supplementary Material Figure S4 that slightly earlier negative peaks could also be chosen for the noise ACFs, which would yield P-wave two-way travel times consistent with that measured from earthquake ACFs.

For each MeSO-net station, we migrate the P-wave two-way travel time values to depth using a constant P-wave velocity of 2.53 km/s. This value corresponds to the JIVSM surface-to-bedrock P-wave velocity averaged over the 287 station locations and is relatively constant within the basin with a one standard deviation to the mean of 0.1 km/s. We show the JIVSM, noise ACF, and earthquake ACF bedrock depths in Figures 4a, 4b, and 4c, respectively. Note that 11 and 17 stations are not displayed in Figures 4b and 4c as no negative peak was found within the theoretical $2p^3 \pm 2.5$ s and $2p \pm 0.65$ s time windows, respectively. Both methods show consistent bedrock depths with the JIVSM, with a shallow bedrock beneath the eastern part of the basin and the mountainous region to the west. The deepest part of the basin is also well retrieved by both the noise and earthquake ACF methods. To quantify the depth differences between the models, we finally compute residuals as the JIVSM bedrock depth minus that from the noise and earthquake ACFs and show them in Figures 4d and 4e, respectively. The mean of the residuals over all the MeSO-net stations (μ) is less than 100 m for both methods and the one standard deviations to the mean (σ) are 290 m and 327 m for the noise and earthquake ACFs, respectively. This confirms that both noise and earthquake ACFs can be used to map the complex shape of the Kanto Basin bedrock.

The major difference between Figures 4d and 4e is the shallower bedrock area in the Tokyo/Yokohama region obtained with earthquake ACFs (e.g., cluster of red circles in Figure 4e). As mentioned above, this region corresponds to the area along Line 4 where earlier negative peaks could also be picked for noise ACFs. This would lead to consistent P-wave two-way travel times for both methods and a bedrock depth that is up to 1.3 km shallower than that predicted by the JIVSM (Supplementary Material Figure S4). Such a shallower bedrock depth in the southern part of the basin is consistent with the results from Yoshimoto et al. (2009), who used the autocorrelation of S-waves from near-field earthquakes to infer the bedrock depth using the same stations. Finally, Denolle et al. (2018) showed that the southern part of the basin is expected to yield strong, complex, and highly variable long-period ground motions during potential future crustal earthquakes. Therefore, future work is required to refine our understanding of the basin structure in this region and better assess seismic hazard.

The noise ACFs computed in the Kanto Basin are relatively different from that in other studies (e.g., Saygin et al., 2017; Romero & Schimmel, 2018; Clayton, 2020) as their frequency content is primarily limited to the 1 to 10 s period range. At higher frequencies (e.g., 1-3 Hz), noise ACFs do not contain any clear surface-to-bedrock phases (Supplementary Material Figure S5). A potential explanation is that the attenuation of high-frequency P-waves in the Kanto Basin is stronger than in other sedimentary basins. This hypothesis is consistent with the weak and noisy high-frequency (1-3 Hz) earthquake ACF phases (Supplementary Material Figure S5), which are generally well retrieved in other regions (e.g., Pham & Tkalčić, 2017). We also note that high-frequency earthquake ACF phases only appear where the $2p^2$ phases are clearly observed in the 1 to 10 s period range (e.g., in the region where the four lines intersect).

To investigate the cause of the multiples observed at some stations, we simulate the elastic wave propagation in layered 2-dimensional media at the HYHM and STHM stations using the SOFI2D package (Supplementary Text and Figure S6 and Table S2, Bohlen et al., 2016). Both stations are located above relatively flat sedimentary layers to limit the unwanted contributions from 3-D wave propagation effects (Figures 1a and 2e). We compute the ACFs of simulated waveforms from two different sources and show that they reproduce well the noise and earthquake ACFs at the two stations. The ACFs at the STHM station, where clear multiples can be observed, have a higher frequency content than that at the HYHM station. The different frequency contents, which are caused by different bedrock depths, make the multiples appear more or less clearly in the ACFs. Therefore, the difference of layer thickness and the bedrock depth at the two station locations can explain the presence (or absence) of P-wave multiples in the noise and earthquake ACFs. However, our 2-D simulations cannot fully reproduce the noise and earthquake ACFs and future work is required to better explain the Kanto Basin structure.

4 Conclusions

We showed that noise and earthquake ACFs computed from the stations of a dense seismic network can be used to image the bedrock of the complex Kanto Basin. Both noise and earthquake ACFs contained clear P-wave reflections from which the P-wave two-way travel time between the surface and the bedrock can be extracted. After migrating the measured P-wave two-way travel time to depth, we confirmed that the bedrock depth obtained with both methods agrees well with that from the JIVSM. Our results also showed that the bedrock in southern part of the basin could be shallower than that predicted by the JIVSM, which could be critical for seismic hazard assessment. Finally, this study is, to our best knowledge, the first to use both noise and earthquake ACFs to map the bedrock shape of an entire basin.

In the future, the results from this study could be combined with the promising results of Chimoto and Yamanaka (2020), who used the autocorrelation of S-waves from nearby earthquakes to compute the S-wave reflectivity response at several sites in the Kanto basin. Moreover, a clear next step of this work is to couple the P- and S- reflectivity responses from ACFs with H/V ratio and/or receiver function analyses to better constrain local 1-D velocity structures. Such results could finally be combined with a classical ambient noise surface-wave tomography to refine images of the Kanto Basin and other sedimentary basins worldwide with dense instrumentation, such as Los Angeles, Seattle, and Mexico City.

Acknowledgments
We thank the MeSO-net project members for the data and Thanh-Son Pham for the earthquake auto-correlation codes and useful discussions. L.V. also thanks Tomotaka Iwata for

useful discussions. The MeSO-net data can be downloaded at `https://www.hinet.bosai.go.jp`. The Python codes to compute noise ACFs and to reproduce Figures 1-4 will soon be made available on GitHub. The Python codes to compute noise ACFs will also be included in the NoisePy Python package (Jiang & Denolle, 2020). L.V. is supported by the JSPS Postdoctoral Fellowship for Research in Japan award number P18108.

References

Anderson, J. G., Bodin, P., Brune, J. N., Prince, J., Singh, S. K., Quaas, R., & Onate, M. (1986). Strong ground motion from the Michoacan, Mexico, earthquake. *Science*, *233*, 1043–1049. doi: 10.1126/science.233.4768.1043

Bensen, G. D., Ritzwoller, M. H., Barmin, M. P., Levshin, A. L., Lin, F., Moschetti, M. P., ... Yang, Y. (2007). Processing seismic ambient noise data to obtain reliable broadband surface wave dispersion measurements. *Geophys. J. Int.*, *169*, 1239–1260. doi: 10.1111/j.1365-246X.2007.03374.x

Bohlen, T., Nil, D. D., Köhn, D., & Jetschny, S. (2016). *Sofi2d seismic modeling with finite differences: 2d – elastic and viscoelastic version* (used under GNU General Public License, Free Software Foundation). Karlsruhe Institute of Technology.

Bonnefoy-Claudet, S., Cotton, F., & Bard, P.-Y. (2006). The nature of noise wavefield and its applications for site effects studies: A literature review. *Earth-Science Reviews*, *79*, 205–227. doi: 10.1016/j.earscirev.2006.07.004

Chimoto, K., & Yamanaka, H. (2020, 07). Tuning S-Wave Velocity Structure of Deep Sedimentary Layers in the Shimousa Region of the Kanto Basin, Japan, Using Autocorrelation of Strong-Motion Records. *Bull. Seismol. Soc. Am.*. doi: 10.1785/0120200156

Claerbout, J. (1968). Synthesis of a layered medium from its acoustic transmission response. *Geophysics*, *33*, 264–269. doi: 10.1190/1.1439927

Clayton, R. W. (2020, 01). Imaging the Subsurface with Ambient Noise Autocorrelations. *Seism. Res. Lett.*, *91*, 930-935. doi: 10.1785/0220190272

Delph, J. R., Levander, A., & Niu, F. (2019). Constraining crustal properties using receiver functions and the autocorrelation of earthquake-generated body waves. *Journal of Geophysical Research: Solid Earth*, *124*(8), 8981–8997. doi: 10.1029/2019JB017929

Denolle, M. A., Boué, P., Hirata, N., & Beroza, G. C. (2018). Strong Shaking Predicted in Tokyo From an Expected M7+ Itoigawa-Shizuoka Earthquake. *J. Geophys. Res. Solid Earth*, *123*, 3968-3992. doi: 10.1029/2017JB015184

Denolle, M. A., Miyake, H., Nakagawa, S., Hirata, N., & Beroza, G. C. (2014). Long-period seismic amplification in the Kanto Basin from the ambient seismic field. *Geophys. Res. Lett.*, *41*, 2319–2325. doi: 10.1002/2014GL059425

Fujiwara, H., Kawai, S., Aoi, S., Morikawa, N., Senna, S., Azuma, H., ... Narita, A. (2012). Some Improvements of Seismic Hazard Assessment based on the 2011 Tohoku Earthquake. *Technical Note of the National Research Institute for Earth Science and Disaster Prevention*, *379*.

Furumura, T., & Hayakawa, T. (2007). Anomalous propagation of long-period ground motions recorded in Tokyo during the 23 October 2004 Mw 6.6 Niigata-ken Chuetsu, Japan, earthquake. *Bull. Seismol. Soc. Am.*, *97*, 863–880. doi: 10.1785/0120060166

Gorbatov, A., Saygin, E., & Kennett, B. L. N. (2013, 12). Crustal properties from seismic station autocorrelograms. *Geophys. J. Int.*, *192*(2), 861-870. doi: 10.1093/gji/ggs064

Guéguen, P., Cornou, C., Garambois, S., & Banton, J. (2007). On the Limitation of the H/V Spectral Ratio Using Seismic Noise as an Exploration Tool: Application to the Grenoble Valley (France), a Small Apex Ratio Basin. *Pure and Applied Geophysics*, *164*(1), 115–134. doi: 10.1007/s00024-006-0151-x

Huang, H.-H., Lin, F.-C., Tsai, V. C., & Koper, K. D. (2015). High-resolution probing of inner core structure with seismic interferometry. *Geophysical Research Letters*, *42*(24), 10–622. doi: 10.1002/2015GL066390

Ito, Y., Shiomi, K., Nakajima, J., & Hino, R. (2012). Autocorrelation analysis of ambient noise in northeastern Japan subduction zone. *Tectonophysics*, *572-573*, 38 - 46. doi:

https://doi.org/10.1016/j.tecto.2011.09.019

Jiang, C., & Denolle, M. A. (2020). NoisePy: A new high-performance python tool for ambient-noise seismology. *Seismological Research Letters*, *91*(3), 1853–1866. doi: 10.1785/0220190364

Kasahara, K., Sakai, S., Morita, Y., Hirata, N., Tsuruoka, H., Nakagawa, S., ... Obara, K. (2009, jan). Development of the Metropolitan Seismic Observation network (MeSO-net) for Detection of Mega-thrust beneath Tokyo Metropolitan Area. *Bull. Earthq. Res. Inst.*, *84*, 71–88.

Kennett, B. L., Engdahl, E., & Buland, R. (1995). Constraints on seismic velocities in the earth from traveltimes. *Geophysical Journal International*, *122*(1), 108–124. doi: 10.1111/j.1365-246X.1995.tb03540.x

Koketsu, K., Hatayama, K., Furumura, T., Ikegami, Y., & Akiyama, S. (2005). Damaging long-period ground motions from the 2003 Mw 8.3 Tokachi-oki, Japan earthquake. *Seismol. Res. Lett.*, *76*, 67–73. doi: 10.1785/gssrl.76.1.67

Koketsu, K., & Kikuchi, M. (2000). Propagation of seismic ground motion in the Kanto basin, Japan. *Science*, *288*, 1237–1239. doi: 10.1126/science.288.5469.1237

Koketsu, K., Miyake, H., Fujiwara, H., & Hashimoto, T. (2008). Progress towards a Japan integrated velocity structure model and long-period ground motion hazard map. *Proceedings of the 14th World Conference on Earthquake Engineering*, S10–038.

Koketsu, K., Miyake, H., & Suzuki, H. (2012). Progress towards a Japan integrated velocity structure model and long-period ground motion hazard map. *Proceedings of the 15th World Conference on Earthquake Engineering*, 1773.

Kudo, K. (1978). The contribution of Love waves to strong ground motions. *Proceedings of the 2nd International Conference on Microzonation*, *2*, 765–776.

Kudo, K. (1980). A study on the contribution of surface wave to strong ground motions. *Proceedings of the 7th World Conference on Earthquake Engineering*, 499–506.

Langston, C. A. (1979). Structure under Mount Rainier, Washington, inferred from teleseismic body waves. *Journal of Geophysical Research: Solid Earth*, *84*(B9), 4749-4762. doi: 10.1029/JB084iB09p04749

Leahy, G. M., Saltzer, R. L., & Schmedes, J. (2012). Imaging the shallow crust with teleseismic receiver functions. *Geophysical Journal International*, *191*, 627-636. doi: 10.1111/j.1365-246X.2012.05615.x

Lin, F.-C., & Tsai, V. C. (2013). Seismic interferometry with antipodal station pairs. *Geophysical Research Letters*, *40*(17), 4609–4613. doi: 10.1002/grl.50907

Liu, G., Persaud, P., & Clayton, R. W. (2018, 08). Structure of the Northern Los Angeles Basins Revealed in Teleseismic Receiver Functions from Short-Term Nodal Seismic Arrays. *Seismological Research Letters*, *89*(5), 1680-1689. doi: 10.1785/0220180071

Mamula, L., Kudo, K., & Shima, E. (1984). Distribution of ground-motion amplification factors as a function of period (3-15 s), in Japan. *Bull. Earthq. Res. Inst.*, *59*, 467–500.

Morrice, D. J., Kenyon, A. S., & Beckett, C. J. (2001). Optimizing operations in 3-d land seismic surveys. *Geophysics*, *66*(6), 1818-1826. doi: 10.1190/1.1487124

Nakamura, Y. (1989). A method for dynamic characteristics estimation of subsurface using microtremor on the ground surface. *Quarterly Report of Railway Tech. Res. Inst.*, *30*, 25–30.

Oren, C., & Nowack, R. L. (2016). Seismic body-wave interferometry using noise autocorrelations for crustal structure. *Geophysical Journal International*, *208*, 321–332. doi: https://doi.org/10.1093/gji/ggw394

Pham, T.-S., & Tkalčić, H. (2017). On the feasibility and use of teleseismic p wave coda autocorrelation for mapping shallow seismic discontinuities. *J. Geophys. Res. Solid Earth*, *122*, 3776-3791. doi: 10.1002/2017JB013975

Phạm, T.-S., & Tkalčić, H. (2018). Antarctic ice properties revealed from teleseismic p wave coda autocorrelation. *Journal of Geophysical Research: Solid Earth*, *123*(9), 7896-7912. doi: 10.1029/2018JB016115

Romero, P., & Schimmel, M. (2018). Mapping the basement of the ebro basin in spain with seismic ambient noise autocorrelations. *J. Geophys. Res. Solid Earth*, *123*, 5052-5067.

doi: 10.1029/2018JB015498
Sakai, S., & Hirata, N. (2009, jan). Distribution of the Metropolitan Seismic Observation network. *Bull. Earthq. Res. Inst.*, *84*, 57–69.
Saygin, E., Cummins, P. R., & Lumley, D. (2017). Retrieval of the P wave reflectivity response from autocorrelation of seismic noise: Jakarta Basin, Indonesia. *Geophys. Res. Lett.*, *44*, 792–799. doi: 10.1002/2016GL071363
Schimmel, M., & Paulssen, H. (1997, 08). Noise reduction and detection of weak, coherent signals through phase-weighted stacks. *Geophys. J. Int.*, *130*, 497-505. doi: 10.1111/j.1365-246X.1997.tb05664.x
Takemura, S., Akatsu, M., Masuda, K., Kajikawa, K., & Yoshimoto, K. (2015). Long-period ground motions in a laterally inhomogeneous large sedimentary basin: observations and model simulations of long-period surface waves in the northern Kanto Basin, Japan. *Earth Planets Space*, *67*, 33. doi: 10.1186/s40623-015-0201-7
Tibuleac, I. M., & von Seggern, D. (2012, 04). Crust-mantle boundary reflectors in Nevada from ambient seismic noise autocorrelations. *Geophys. J. Int.*, *189*(1), 493-500. doi: 10.1111/j.1365-246X.2011.05336.x
Tkalčić, H., Phạm, T.-S., & Wang, S. (2020). The earth's coda correlation wavefield: Rise of the new paradigm and recent advances. *Earth-Science Reviews*, 103285. doi: 10.1016/j.earscirev.2020.103285
Tork Qashqai, M., Saygin, E., & Kennett, B. (2019). Crustal imaging with Bayesian inversion of teleseismic P wave coda autocorrelation. *Journal of Geophysical Research: Solid Earth*, *124*(6), 5888–5906.
Viens, L., Koketsu, K., Miyake, H., Sakai, S., & Nakagawa, S. (2016). Basin-scale Green's functions from the ambient seismic field recorded by MeSO-net stations. *J. Geophys. Res. Solid Earth*, *121*, 2507–2520. doi: 10.1002/2016JB012796
Wang, T., Song, X., & Xia, H. H. (2015). Equatorial anisotropy in the inner part of earth's inner core from autocorrelation of earthquake coda. *Nature Geoscience*, *8*(3), 224–227.
Wapenaar, K. (2003). Synthesis of an inhomogeneous medium from its acoustic transmission response. *Geophysics*, *68*, 1756–1759. doi: https://doi.org/10.1190/1.1620649
Yamada, N., & Yamanaka, H. (2012). 3d s-wave velocity model of kanto basin for long-period ground motion simulation with special focus on treatment of shallow near-surface part. *Butsuri Tansa (Geophysical Exploration)*, *65*(3), 139-150. doi: 10.3124/segj.65.139
Yoshimoto, K., Sakurai, K., Nakahara, H., Kinoshita, S., & Sato, H. (2009). Seismic basement structure beneath the Kanto plain, Japan inferred from the seismic interferometry for strong motion records. In *Symposium on "seismic wave scattering and noise correlation"*. Tohoku University.
Yoshimoto, K., & Takemura, S. (2014). Surface wave excitation at the northern edge of the Kanto Basin, Japan. *Earth, Planets and Space*, *66*(1), 16. doi: 10.1186/1880-5981-66-16

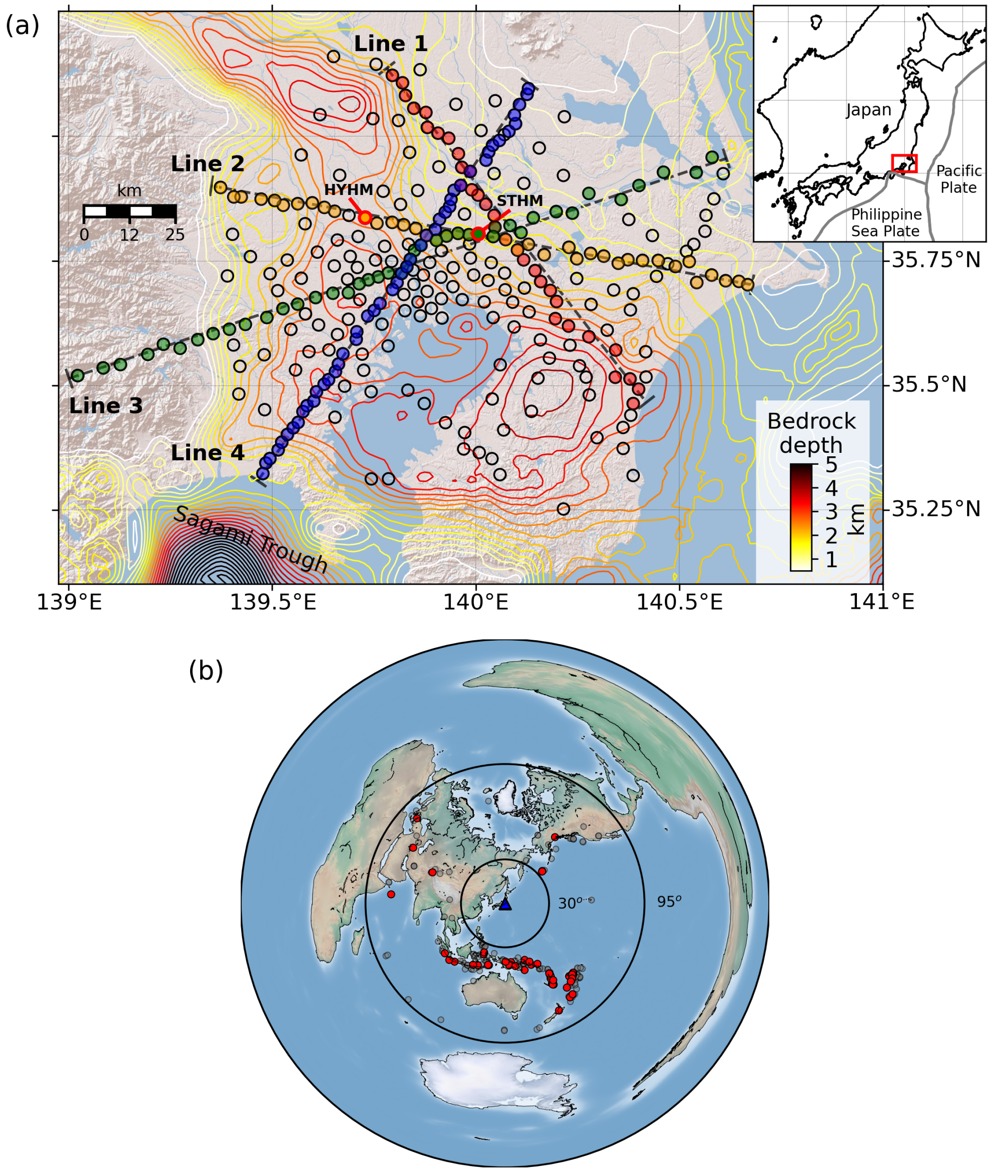

Figure 1. (a) Topographic map of Kanto region including the 287 MeSO-net stations (circles) and 250-m-spaced bedrock iso-depth contours (V_P = 5.5 km/s) from the JIVSM (colored lines, Koketsu et al., 2008, 2012). The stations aligned along Line 1 (red), Line 2 (orange), Line 3 (green), and Line 4 (purple) are also highlighted. The HYHM and STHM station locations are shown by the red edge circles. The four JIVSM profiles in Figures 2 and 3 are taken along the back dashed lines. The inset map shows the Japanese Islands (black lines), the region of interest (red rectangle), and the plate boundaries (gray lines). (b) Azimuthal equidistant projection map centered on the Kanto Basin including the 244 M_w 6+ earthquakes which occurred within 30 and 95 degrees from the Kanto Basin between May 2017 and 2020 (gray circles). The locations of the 50 selected earthquakes are shown by red circles.

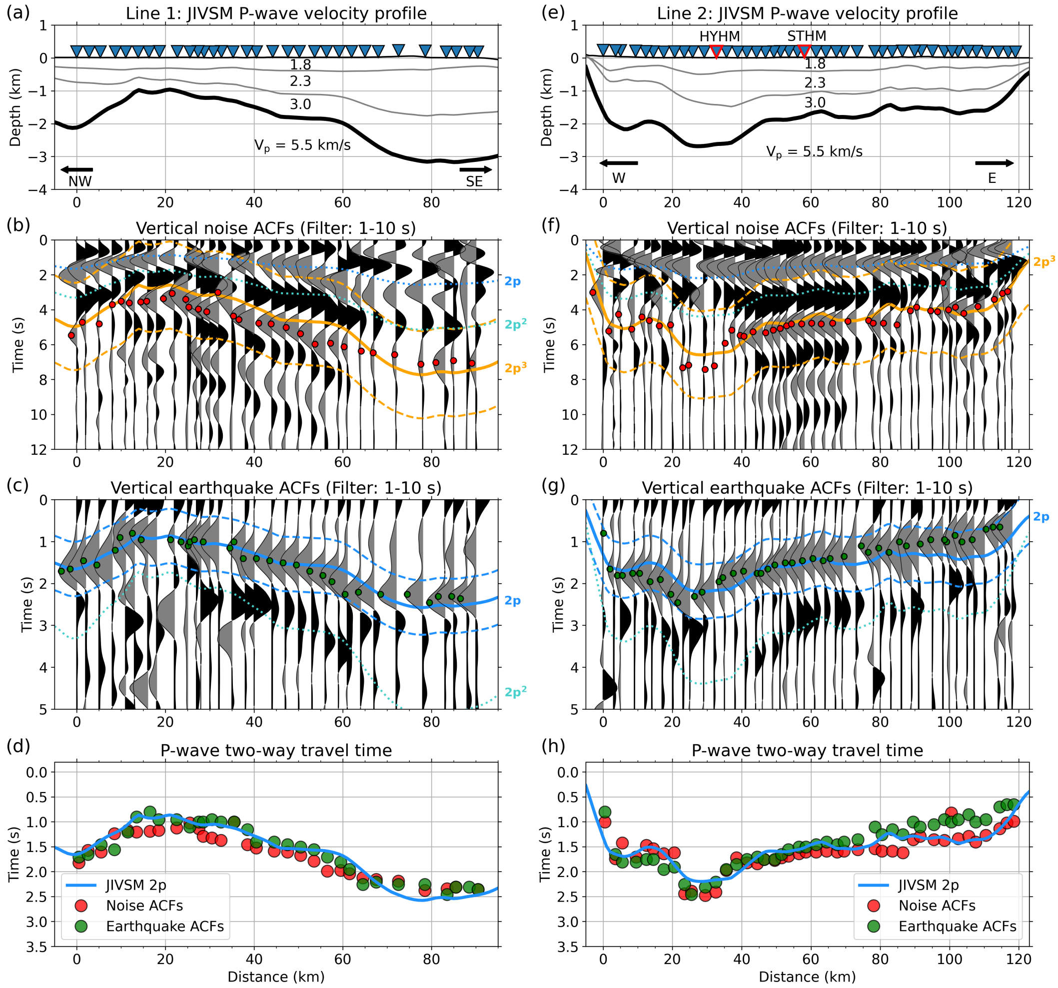

Figure 2. (a) JIVSM velocity profile along Line 1 including the P-wave velocity of each layer. The basin bedrock is highlighted by the thick black line and the orientation of the profile is also indicated (e.g., NW: north-west; SE: south-east). (b) Noise ACFs along Line 1 bandpass filtered between 1 and 10 s. The dotted blue and light blue lines highlight the theoretical $2p$ and $2p^2$ arrival times between the surface and the bedrock, respectively. The thick orange line shows the theoretical $2p^3$ arrival time and the dashed orange lines are the $2p^3$ arrivals ±2.5 s. The red filled circles are the selected negative peaks used in this study. (c) Earthquake ACFs bandpass filtered between 1 and 10 s. The thick blue and dotted light blue lines represent the theoretical $2p$ and $2p^2$ arrival times. The dashed blue lines are the blue line ± 0.65 s. The green dots are the negative peaks selected in this study. Note that the vertical time axes in (b) and (c) are different. (d) Theoretical P-wave two-way travel time (2p, blue line) and the values obtained from noise ACFs divided by three (red circles) and that from earthquake ACFs (green circles). (e-h) Same as (a-d) for Line 2. The HYHM and STHM station locations along Line 2 are also indicated.

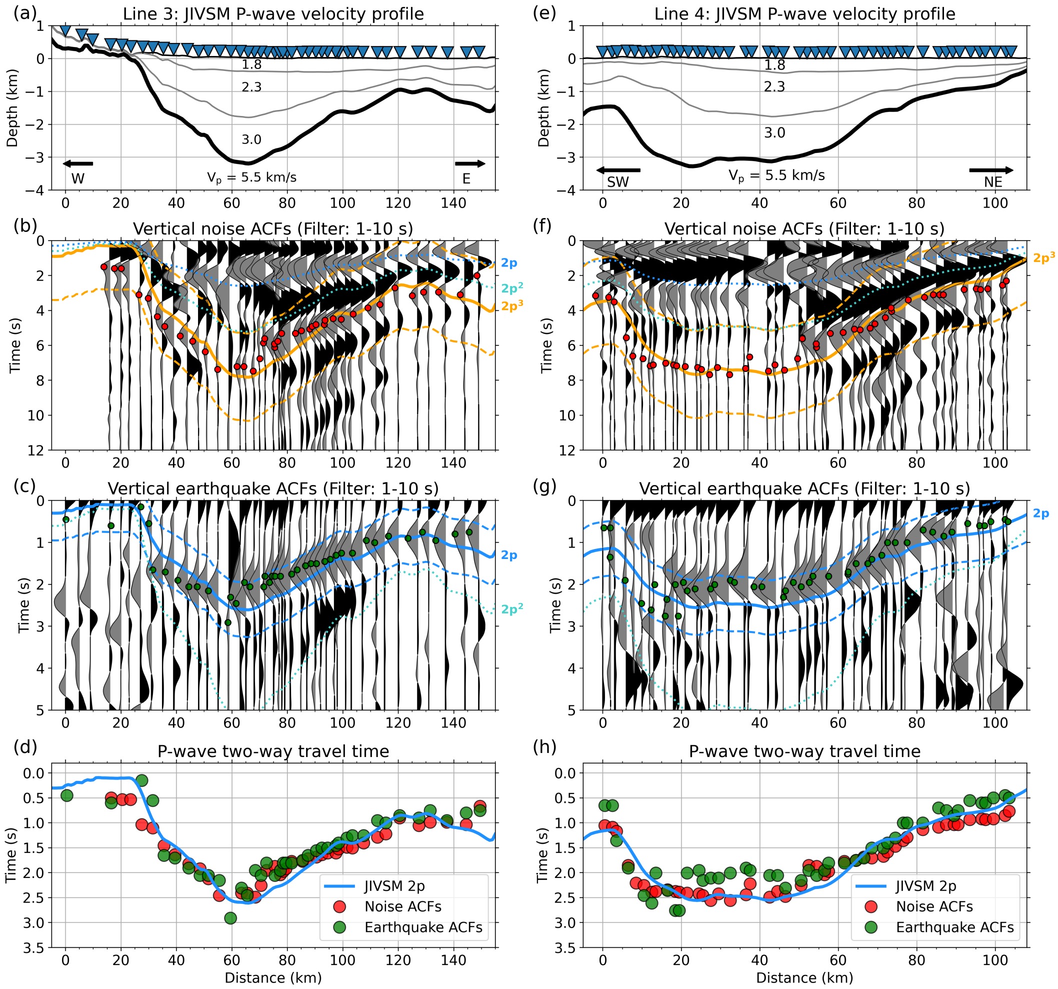

Figure 3. Same as Figure 2 for the stations along Line 3 (a-d) and Line 4 (e-h).

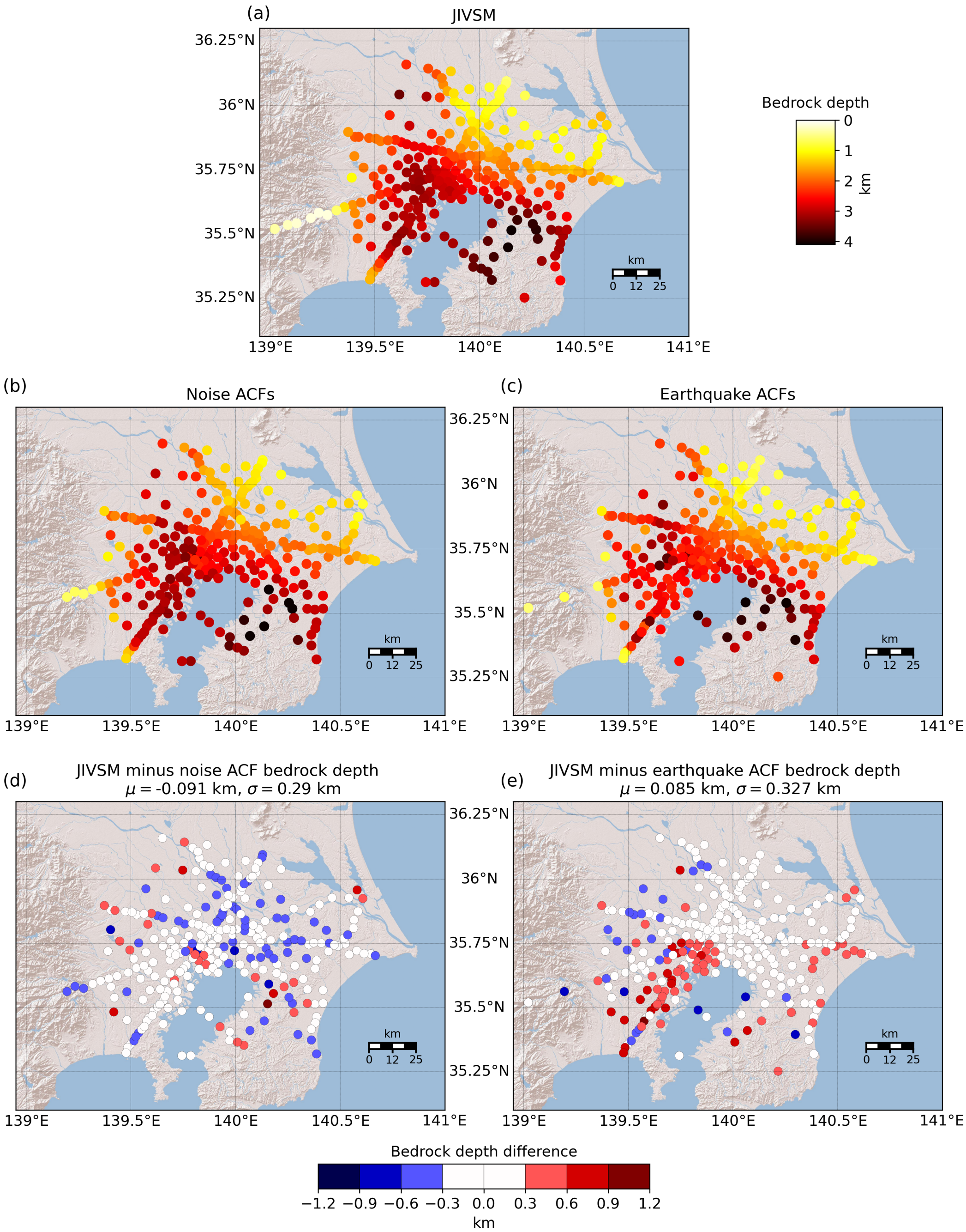

Figure 4. Basin bedrock depth beneath each station from (a) the JIVSM, (b) noise ACFs, and (c) earthquake ACFs. The noise and earthquake bedrock depths are obtained by migrating the P-wave two-way travel times to depth with a constant P-wave velocity of 2.53 km/s. Residuals between the JIVSM bedrock depth minus that from (d) noise ACFs and (e) earthquake ACFs. Blue and red filled circles indicate that the JIVSM bedrock depths are shallower and deeper than that from the ACFs, respectively. The mean of the residuals over all the stations (μ) and the one standard deviation to the mean (σ) are also indicated.

Supporting Information for "Imaging the Kanto Basin bedrock with noise and earthquake autocorrelations"

Loïc Viens[1], Chengxin Jiang[2], and Marine A. Denolle[3]

[1]Disaster Prevention Research Institute, Kyoto University, Uji, Japan

[2]Research School of Earth Sciences, The Australian National University, Canberra, ACT, Australia

[3]Department of Earth and Planetary Sciences, Harvard University, Cambridge, MA, USA

Contents of this file

1. Texts S1 to S6
2. Figures S1 to S6
3. Tables S1 and S2

Corresponding author: Loïc Viens, Disaster Prevention Research Institute, Kyoto University, Uji, Japan (viens.loic.58r@st.kyoto-u.ac.jp)

Introduction

The supporting information includes:

1. Text and Figure S1 discussing the seasonal stability of the noise autocorrelation functions (ACFs)

2. Text and Figure S2 showing the effect of the average trace removal for the stations along Line 1

3. Text and Figure S3 showing the effect of the length of the sliding-spectral windows on earthquake ACFs.

4. Text and Figure S4 showing noise and earthquake ACFs with clipped amplitudes along Line 4

5. Text and Figure S5 showing the noise and earthquake ACFs in the 0.33-1 s (1-3 Hz) period range

6. Table S1 showing the station names and locations for which the noise ACF $2p^3$ values are manually picked

7. Text and Figure S6 and Table S2 showing the results of the 2-D SOFI2D simulations.

Text S1.

To demonstrate the stability of noise ACFs with seasonality, we independently stack the 20-min ACFs for the 2-week periods of January and July with the phase-weighted stack (PWS) method (Schimmel & Paulssen, 1997). We show the noise ACFs as well a the selected negative peak values between the theoretical $2p^3$ phase ± 2.5 s from the JIVSM for the stations along Line 1 in Figure S1. The P-wave two-way travel times obtained independently from the January and July data are consistent with that from the stack over the entire dataset.

We also compare the difference between the JIVSM and January/July noise ACF bedrock depths over the entire network after migrating the P-wave two-way travel times from the noise ACFs to depth using a constant P-wave velocity of 2.53 km/s (e.g., average of the surface-to-bedrock P-wave velocity from the JIVSM over the 287 station locations). For the January noise ACFs, the mean of the depth difference with the JIVSM (μ) is -0.09 km and the one standard deviation (σ) is 0.28 km. For the July noise ACFs, μ is equal to -0.12 km and σ is 0.29 km. These values are very similar to that obtained with the stack over the entire dataset shown in the main manuscript ($\mu = -0.091$ km and $\sigma = 0.290$ km), confirming that noise ACFs are relatively stable through the year.

Text S2.

In Figure S2, we show the effect of the average trace removal on the noise ACFs for the stations along Line 1. The raw noise ACFs are primarily dominated by the near zero-time-lag spikes. By removing an average trace to each ACF, we remove the effect of the source function and enhance the signal-to-noise ratio of the reflectivity response.

Text S3.

Earthquake spectra are pre-whitened using the running-mean average algorithm of Bensen et al. (2007) before computing earthquake ACFs. In the main manuscript, we present the results using a sliding-spectral window of 30 samples (i.e., 0.67 Hz). In the

Supplementary material, we also compute earthquake ACFs with sliding-spectral window of 20 and 45 samples. For the 20-, 30-, and 45-sample sliding-spectral windows, we first measure the two-way travel times from the earthquake ACFs within the theoretical 2p arrival time ± 0.65 s time window. We then migrate the two-way travel times to depth using a constant P-wave velocity of 2.53 km/s and show the bedrock depth maps in Supplementary Material Figure S3. The maps have similar bedrock depths and similar lateral variations. For the 20- and 45-sample sliding-spectral windows, the means of the depth residuals with the JIVSM (μ) are 0.057 km and 0.085 km and the standard deviations to the mean (σ) are 0.334 km and 0.314 km, respectively. These values are very similar to that obtained with a 30-sample sliding-spectral window ($\mu = 0.085$ km and $\sigma = 0.327$ km), which confirms that the degree of smoothing does not significantly impact our results. Finally, a 30-sample sliding-spectral window allows us to measure the 2p travel time at more stations (e.g., 270 out of 287 stations) than if 20- or 45-sample sliding-spectral windows are used (e.g., 259 and 268 out of 287 stations, respectively).

Text S4.

In Figure S4, we show the noise and earthquake ACFs along Line 4 and clip their amplitudes for visibility. In Figure S4b, a clear consistent phase near the theoretical $2p^3$ phase can be observed along Line 4 after clipping the waveforms amplitudes, which is not the case in Figure 3f of the main manuscript. Moreover, several negative peaks can be observed within the theoretical $2p^3 \pm 2.5$ s time window between 20 to 50 km from the south-western end of Line 4. In the main manuscript, we automatically select the negative peaks that are the closest to the theoretical $2p^3$ phase. In Figures S4b and S4d, we show that by selecting ∼0.5 to 1 s earlier negative peaks, the resulting P-wave two-way travel times are very similar to that obtained from the earthquake ACFs. This indicates that the basin bedrock could be up to 1.3 km shallower than that predicted by the JIVSM in this region by considering a constant P-wave velocity of 2.53 km/s.

Text S5.

In Figure S5, we show the noise and earthquake ACFs in the 0.33 to 1 s period range (e.g., 1–3 Hz) at the stations along Lines 3 and 4. For both methods, the only difference with the main manuscript is the frequency range of the bandpass filter applied after autocorrelating and stacking the waveforms. The high-frequency noise ACFs do not show any clear phases near the theoretical 2p, $2p^2$, and $2p^3$ arrival times. On the other hand, the high-frequency earthquake ACFs have clear arrivals near the theoretical 2p arrival time in some parts of the basin (e.g., mainly where the four lines intersect), but are noisier than in the 1 and 10 s period range.

Text S6.

To explain the presence (or absence) of the multiples observed at some stations in the noise and earthquake ACFs, we simulate the elastic wave propagation in layered 2-dimensional media with the finite difference modeling SOFI2D package (Figure S6, Bohlen et al., 2016). The velocity models are taken from the JIVSM at the location of the HYHM and STHM stations, which are located above relatively flat sedimentary layers to limit the unwanted contributions from 3-D wave propagation effects.

The two velocity models are shown in Figures S6a and S6e and detailed in Table S2. Note that the top boundary is the free surface and the sides and bottom (depth: 25 km) of the model have perfectly matched layers to damp the waves and avoid reflections. For the two models, a receiver is located at a depth of 20 meters. To simulate the noise and earthquake ACFs, we use Ricker source functions with a dominant frequency of 2 Hz (0.5 s) located at two different depths: 20 m to reproduce the noise ACF and 20 km to reproduce the earthquake ACF and simulate the near vertical incidence of teleseismic P waves.

The waveforms of the deep and surface sources recorded at the station for the two velocity models are shown in Figures S6b and S6f. For the HYHM and STHM stations, we bandpass filter the synthetic waveforms between 4 and 10 s and 3 and 10 s, respectively. We focus on slightly different period ranges as the noise and earthquake ACFs at the two stations have different predominant period ranges, with the ACFs at the HYHM stations having a lower frequency content compared to that at the STHM station.

In the following, the 40-s waveform recorded at the surface station is considered for the deep source as earthquake ACFs contain the direct P-waves and their coda. For the shallow source, however, we only consider the part of the waveforms after approximately 9 s (after the green dashed lines in Figure S6b and S6f), as the ambient noise generally does not contain any strong direct arrivals. The considered synthetic waveforms are then autocorrelated in the frequency domain after zero-padding them to four times their original duration. Finally, we taper the first 0.5 s of the causal part of the simulated ACFs and normalize their amplitudes.

We show the simulated with the deep source and earthquake ACFs for the two stations in Figures S6c and S6g. For both stations, the simulated ACFs reproduce relatively well the earthquake ACFs. The first negative peak of the earthquake ACFs (Figures S6c and S6g), which corresponds to the 2p arrival time, is well retrieved. Moreover, the following positive peak, which we attribute to the $2p^2$ arrival time in the main manuscript, is also retrieved. More interestingly, the higher frequency content of the ACF at the STHM station makes the $2p^2$ phase appear more clearly compared to that at the HYHM station. This is coherent with the earthquake ACFs at the two stations, with the earthquake ACF at the STHM station having a stronger $2p^2$ phase compared to that at the HYHM station. Therefore, the difference of layer thickness and the bedrock depth can explain the presence (or absence) of P-wave multiples in the earthquake ACFs through a different frequency content.

In Figures S6d and S6h, we show the simulated with the surface source and noise ACFs for the two stations. Similarly to the earthquake ACFs, the simulated ACFs reproduce well the noise ACFs at the two stations and the $2p^3$ phase is also well retrieved. Moreover, the simulated ACF at the HYHM station has fewer multiples than that at the STHM station, which is consistent with the noise ACFs. For both stations, the noise ACF phases are also slightly delayed compared to that of the simulations, which is consistent with the slightly delayed measured P-wave two-way travel times shown in Figure 2h.

While the simulated ACFs reproduce well the noise and earthquake ACFs, some differences in terms of both phase and amplitude of the waveforms can be observed, which we can be attributed to following factors. 1) The layered 2-D velocity models might be too simple and do not capture 3-D wave propagation effects. 2) The internal layering from the JIVSM (above the seismic basement) may not be accurate enough.

References

Bensen, G. D., Ritzwoller, M. H., Barmin, M. P., Levshin, A. L., Lin, F., Moschetti, M. P., … Yang, Y. (2007). Processing seismic ambient noise data to obtain reliable broad-band surface wave dispersion measurements. *Geophys. J. Int.*, *169*, 1239–1260. doi: 10.1111/j.1365-246X.2007.03374.x

Bohlen, T., Nil, D. D., Köhn, D., & Jetschny, S. (2016). *Sofi2d seismic modeling with finite differences: 2d – elastic and viscoelastic version* (used under GNU General Public License, Free Software Foundation). Karlsruhe Institute of Technology.

Schimmel, M., & Paulssen, H. (1997, 08). Noise reduction and detection of weak, coherent signals through phase-weighted stacks. *Geophys. J. Int.*, *130*, 497-505. doi: 10.1111/j.1365-246X.1997.tb05664.x

Table S1: List of stations where the negative peaks of noise ACF near the theoretical $2p^3$ arrival time are manually adjusted.

Station name	Latitude	Longitude
KMHM	35.37081	139.51450
KSGM	35.72642	139.78508
KYTM	35.55539	140.18094
NBKM	35.95800	140.58061
SMGM	35.38658	139.52344
TMHM	35.51506	140.15281
YYIM	35.71855	139.76035

Table S2: Details of the two velocity models used in Figure S6. The "JIVSM layer depth" column shows the depth of the top and bottom of each layer in kilometers. The "used layer depths" are slightly different due to computational constrains. Vp, Vs, and ρ are the P-wave and S-wave velocities and the density of each layer, respectively.

Model	JIVSM layer depth (km)	Used layer depth (km)	Vp (km/s)	Vs (km/s)	ρ (g/cm^3)
Model 1 HYHM station	0.00–0.400	0.00–0.40	1.8	0.5	1.95
	0.400–1.455	0.40–1.46	2.3	0.9	2.1
	1.455–2.667	1.46–2.67	3.0	1.5	2.25
	2.667–25.000	2.67–25.00	5.5	3.2	2.65
Model 2 STHM station	0.0–0.420	0.0–0.42	1.8	0.5	1.95
	0.420–1.104	0.42–1.10	2.3	0.9	2.1
	1.104–1.788	1.10–1.78	3.0	1.5	2.25
	1.788–25.000	1.78–25.00	5.5	3.2	2.65

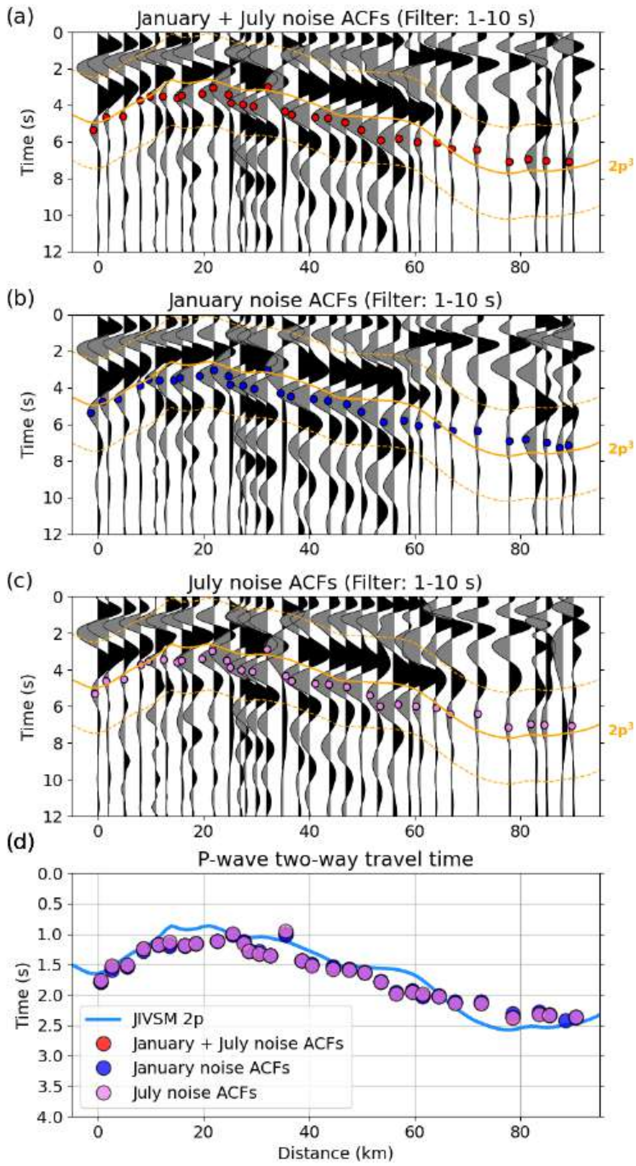

Figure S1: Noise ACFs along Line 1 computed from the data recorded in (a) January and July (e.g., main manuscript), (b) January, and (c) July. All the ACFs are bandpass filtered between 1 and 10 s and an average trace has been subtracted to each ACF to enhance the reflectivity response. The thick orange lines represent the theoretical $2p^3$ arrivals from the JIVSM and the dashed orange lines are the $2p^3$ arrivals ± 2.5 s. The selected negative peaks are shown by the red, blue, and purple filled circles. (d) Theoretical P-wave two-way travel time from the JIVSM (2p, blue line) and the values obtained from (a), (b), and (c) divided by 3 (colored circles).

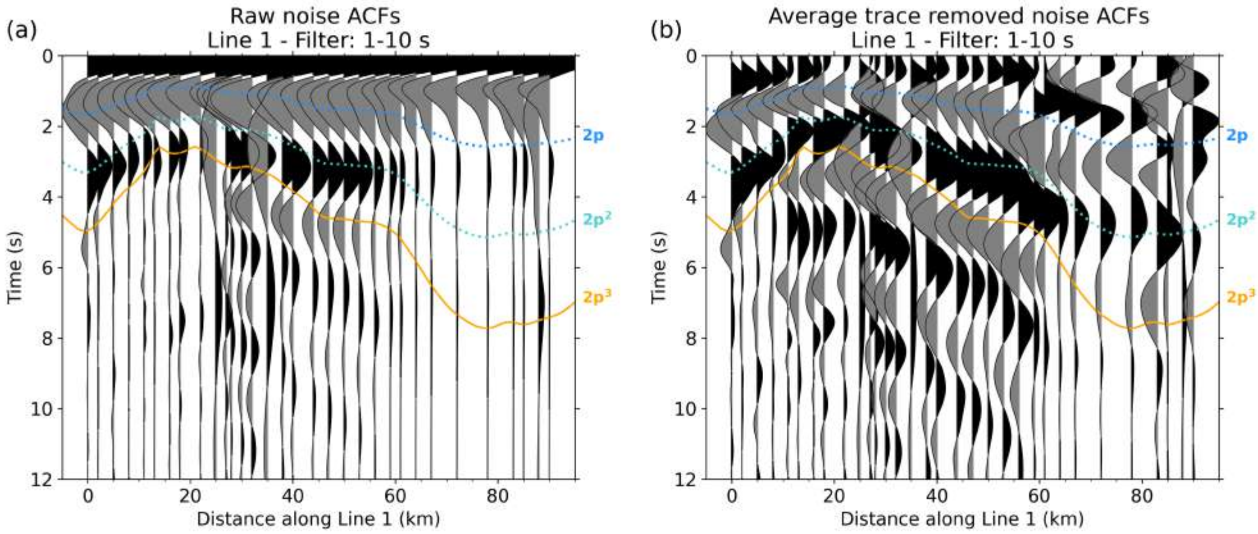

Figure S2: (a) Raw noise ACFs along Line 1 computed over the 30 days of continuous vertical records. (b) Noise ACFs along Line 1 after removing an average trace to each noise ACF. All the waveforms are normalized by their peak absolute amplitude. The amplitude of the waveforms in (a) is 3 times that of the waveforms in (b) for visibility. The blue, light blue, and orange lines represent the theoretical 2p, $2p^2$, and $2p^3$ arrival times from the JIVSM. All the ACFs are bandpass filtered between 1 and 10 s.

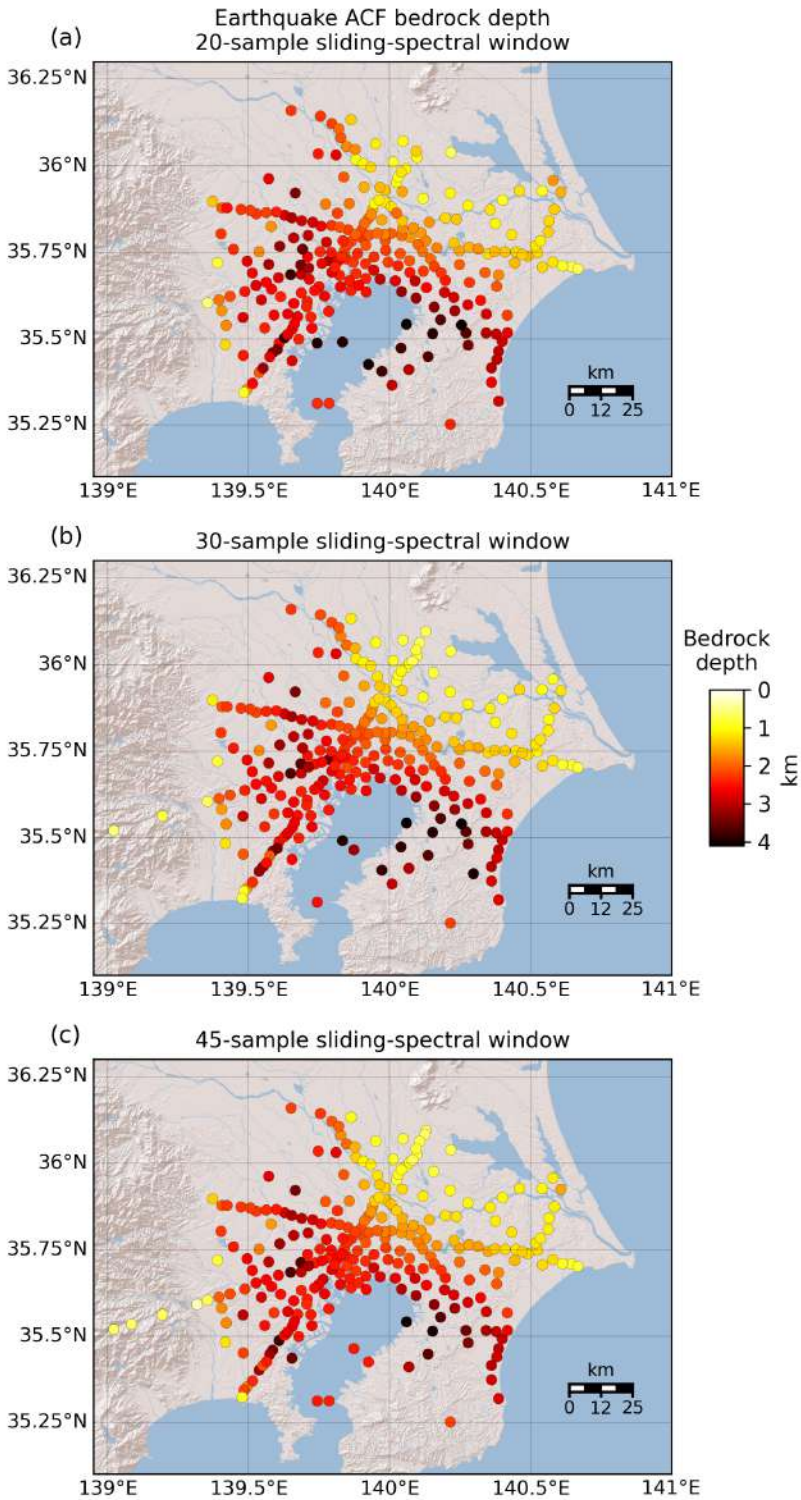

Figure S3: Earthquake ACF bedrock depths obtained with pre-whitening sliding-spectral windows of (a) 20-, (b) 30-, and (c) 45-samples. The bedrock depths are obtained by migrating the two-way travel times measured from earthquake ACFs to depth using a constant P-wave velocity of 2.53 km/s. Note that 259, 270, and 268 stations (out of 287) are used in (a), (b), and (c), respectively, as some waveforms do not contain any negative peaks within the theoretical 2p arrival time ±0.65 s time window.

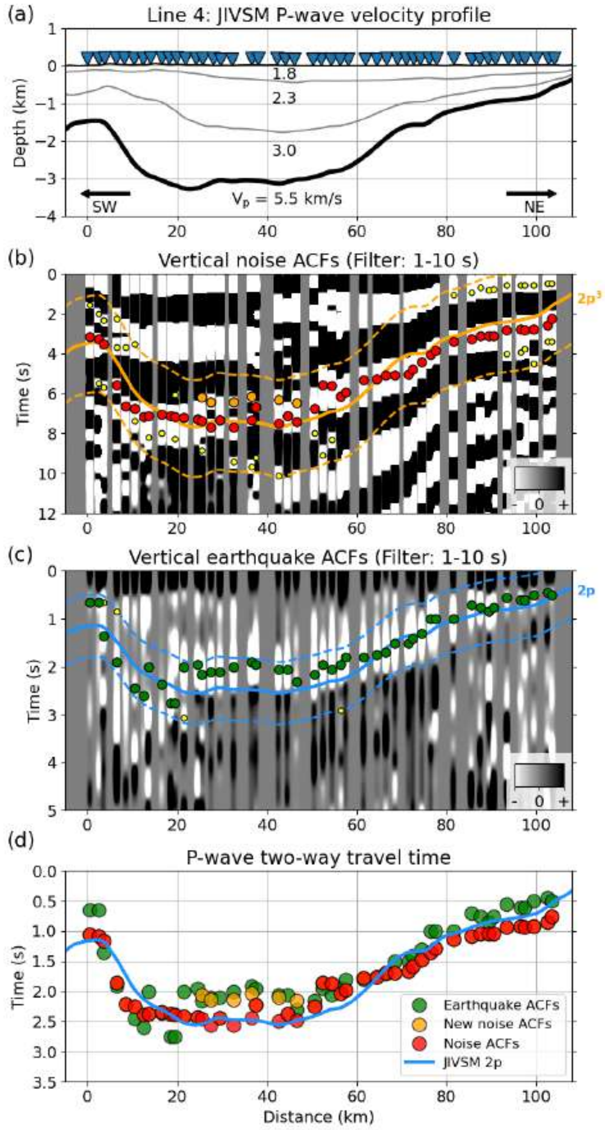

Figure S4: (a) JIVSM P-wave velocity profile along Line 4. (b) Noise ACFs along Line 4 bandpass filtered between 1 and 10 s with clipped amplitudes for visibility. The orange thick and dashed lines highlight the theoretical $2p^3$ arrival time and the $2p^3$ arrival ± 2.5 s, respectively. The red and orange filled circles are the negative peaks used in the main manuscript and in the Supplementary Material Text S4, respectively. The yellow filled circles are other negative peaks found within the theoretical $2p^3$ arrivals ± 2.5 s window. (c) Vertical earthquake ACFs filtered between 1 and 10 s with clipped amplitudes for visibility. The blue line represents the theoretical 2p arrival time and the dashed lines are the blue line $\pm$ 0.65 s. The green dots are the negative peaks selected within the considered time window. Note that the vertical time axes in (b) and (c) are different. (d) Theoretical P-wave two-way travel time (2p, blue line), measured 2p travel time from earthquake ACFs (green circles), measured noise ACF values within the theoretical $2p^3 \pm 2.5$ s window divided by 3 (red circles, used in the main manuscript), and early noise ACF measurements discussed in Supplementary Material Text S4 (orange circles).

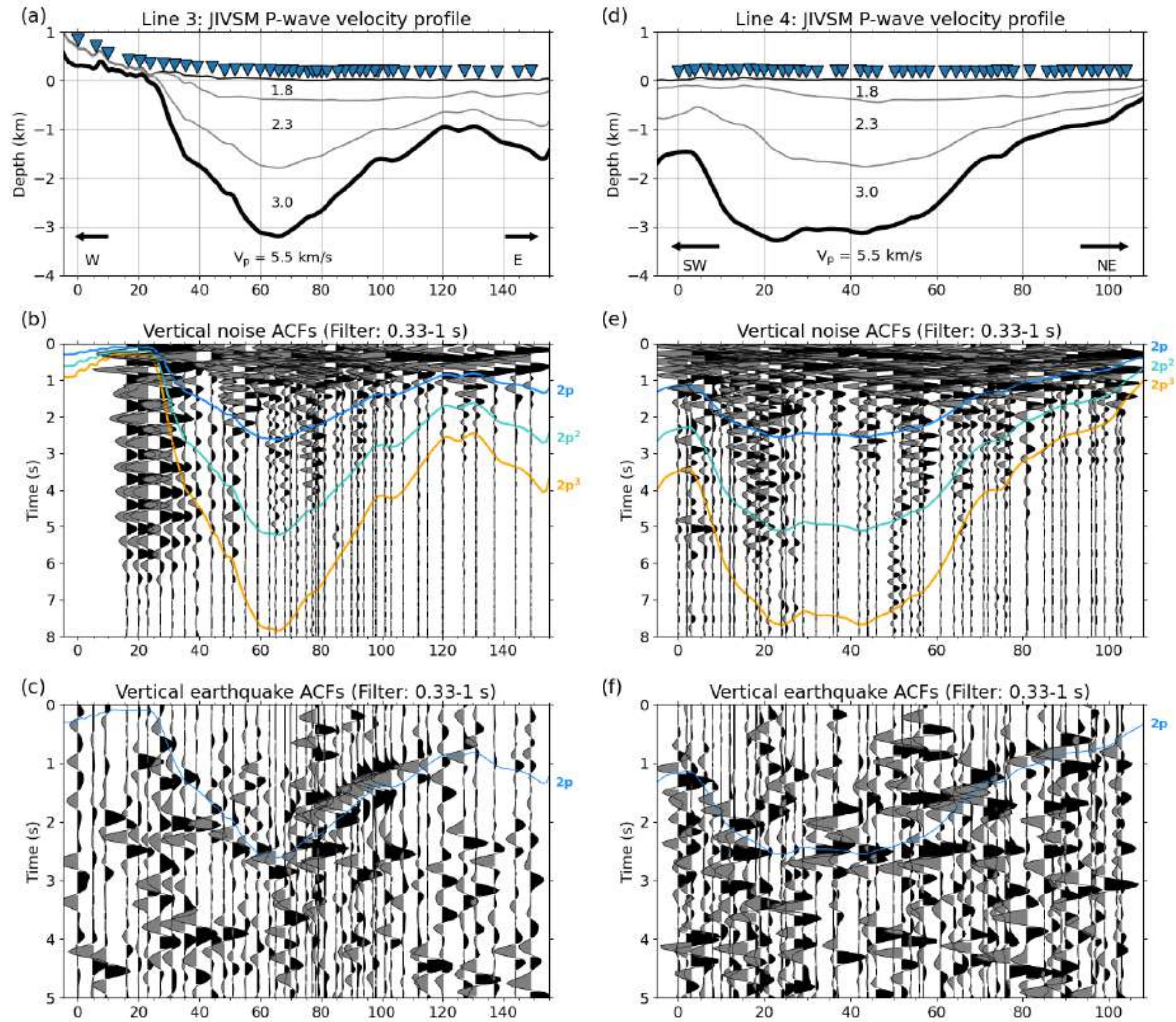

Figure S5: (a) JIVSM P-wave velocity profile along Line 3. (b) Noise ACFs bandpass filtered between 0.33 and 1 s (1-3 Hz) for the stations along Line 3. The theoretical 2p, $2p^2$, and $2p^3$ arrival times from the JIVSM are also highlighted. (c) Earthquake ACFs bandpass filtered between 0.33 and 1 s (1-3 Hz) for the stations along Line 3. (e-f) Same as (a-c) for the stations along Line 4.

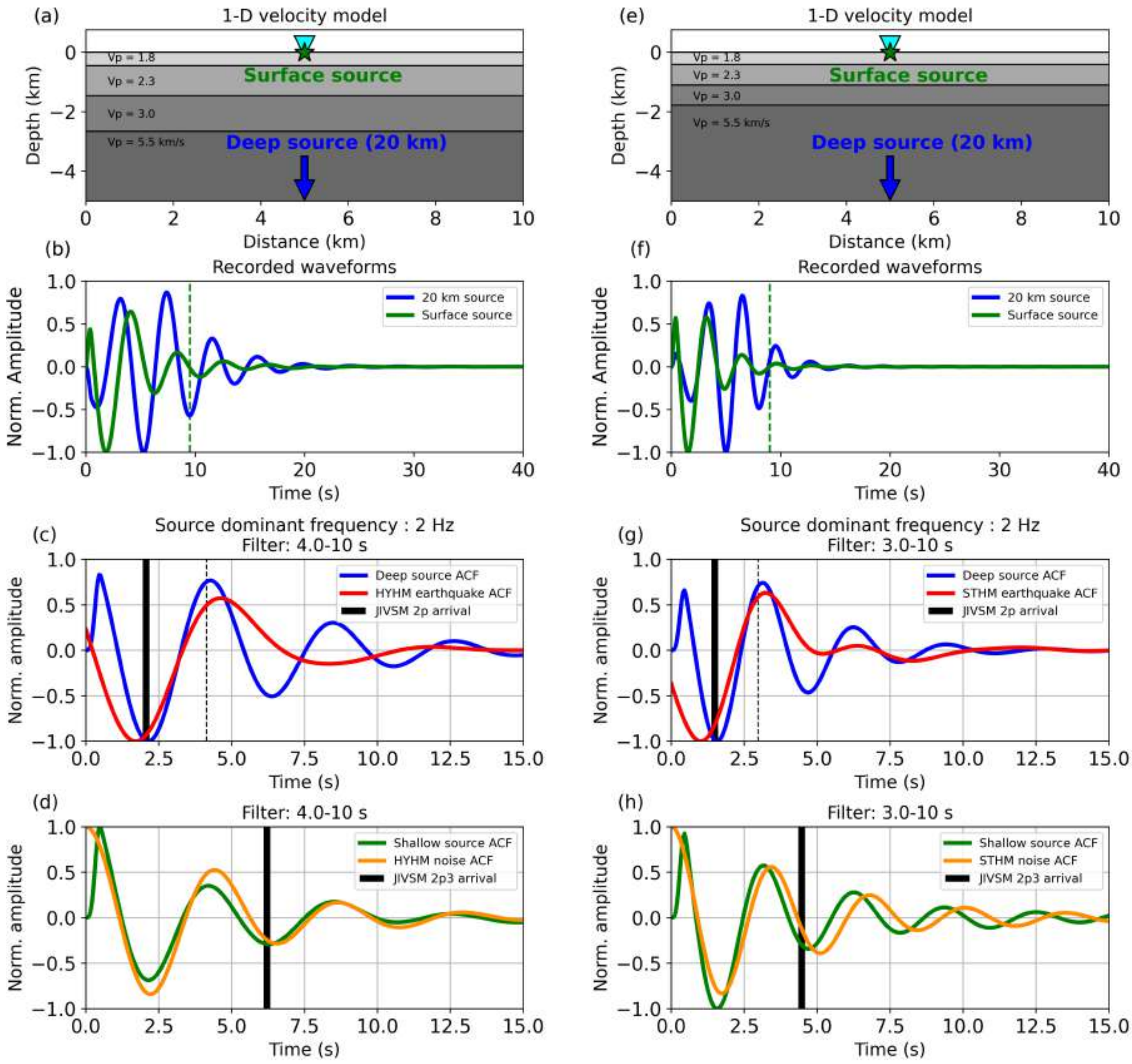

Figure S6: (a) 2-D velocity model used for the SOFI2D simulations at the HYHM station, including the surface and deep source locations of the Ricker functions (green start and blue arrow) and the recording station (inverted blue triangle). (b) Recorded waveforms from the surface and deep sources at the station (green and blue traces). For the surface source, only the part of the waveform after the vertical green dashed line is considered to compute the simulated ACF shown in (d). (c) ACF of the simulated waveform from the deep source (blue trace), earthquake ACF at the HYHM station (red trace), and theoretical 2p and $2p^2$ arrival times (vertical black thick and dashed lines) from the JIVSM calculated from the 2-D velocity model in (a). (d) ACF of the simulated waveform from the shallow source (green trace), noise ACFs at the HYHM station (orange trace), and theoretical $2p^3$ arrival from the JIVSM from the 2-D velocity model in (a). (e-h) Same as (a-d) for the velocity model below the STHM station. Note that the period range in (g) and (h) is slightly different from that in (c) and (d).